Journal of Water Process Engineering 77 (2025) 108635

Contents lists available at ScienceDirect

Journal of Water Process Engineering

journal homepage: www.elsevier.com/locate/jwpe

Perfluoroalkyl substances (PFAS) rejection with plasma polymerized ultrafiltration membranes☆

Jingshi Wang [a], Priyanka Kumari [b], Jitraporn Vongsvivut [c], Andrea Merenda [d], Jiangting Wang [a], Zhiqiang Chen [a], Ilana Timokhina [e], Ludovic F. Dumée [f,g,*], Lingxue Kong [a]

[a] Institute for Frontier Materials, Deakin University, Geelong, VIC 3216, Australia
[b] Khalifa University, Department of Chemical and Petroleum Engineering, Abu Dhabi, United Arab Emirates
[c] Infrared Microspectroscopy (IRM) Beamline, ANSTO – Australian Synchrotron, Clayton, VIC 3168, Australia
[d] School of Civil and Environmental Engineering, University of Technology, Sydney (UTS), City Campus, Broadway, NSW 2007, Australia
[e] Lulea University of Technology, Sweden
[f] Element Zero, Department of Research and Innovation, Malaga, Western Australia, Australia
[g] State Key Laboratory of Materials-Oriented Chemical Engineering, National Engineering Research Center for Special Separation Membrane, Nanjing Tech University, Nanjing, China

ARTICLE INFO

Editor: Luca Fortunato

Keywords:
Plasma polymerization
Acrylic acid (AAc)
Tight-pore membranes
PFAS removal
Antifouling performance

ABSTRACT

This work investigated the efficient routes for the fabrication of semi-permeable thin films for desalination using plasma polymerization technology. Acrylic acid (AAc) was selected as a precursor for plasma polymerization due to its hydrophilic properties and potential for low fouling functionalization and ability to form flexible, filtration-ready films. The plasma polymerized AAc films were deposited on the top of poly(sulfone) ultrafiltration (PSf UF) membranes to enhance the selectivity of the composite membranes. Different plasma modes such as continuous wave (CW) or pulsed plasma were applied to overcome the brittleness issue. Such narrow pore size UF membranes, with pores less than 10 nm, were further used for rejecting perfluoroalkyl substances (PFASs), a class of persistent environmental chemicals, also known as an emerging threat to public health and the environment. The selectivity and antifouling behavior of the tight UF membranes were investigated against four PFASs differentiated by molecular weight. The tight UF membranes have shown approximately 20 % higher rejection than the pristine PSf. Although the rejection rate was enhanced proportionally with the size of PFAS compounds, membrane fouling became severe as the size of PFAS became close to the molecular cut-off size of the composite membranes. The surfaces of the tight UF plasma modified membranes were more hydrophilic with a water contact angle of 15.1° and negatively charged streaming potential of −31 mV at pH 8, which contributed to the lowest total permeance decline ratio and highest flux recovery rate compared with pristine PSf during each filtration test. The outcome of this study has opened more opportunities for the application of the plasma polymerized membranes for gas separation, water treatment, fuel cells, biomedical devices, and protective coatings.

1. Introduction

Per- and polyfluoroalkyl substances (PFAS) are a class of synthetic chemicals widely used in industrial and consumer products for their water- and oil-resistant properties. However, their chemical stability makes them highly persistent in the environment and difficult to remove from water, posing serious health and ecological concerns [1]. High selectivity polymer membranes, such as ultrafiltration (UF), nanofiltration (NF), and reverse osmosis (RO) membranes, are popular for their ability to efficiently remove molecular compounds such as metallic ions, organic molecules, salts and microbes from wastewater [2,3]. The performance of such systems is governed by both the intrinsic properties of the selective layer such as chemical composition, cross-linking density, surface roughness, and wettability and the operating conditions, including temperature, pressure, feed composition, and flow dynamics [4,5]. Material properties such as wettability and adsorption

☆ This article is part of a Special issue entitled: 'PFAS Management' published in Journal of Water Process Engineering.

* Corresponding author at: Element Zero, Department of Research and Innovation, Malaga, Western Australia, Australia.
E-mail address: ludo@elementzero.green (L.F. Dumée).

https://doi.org/10.1016/j.jwpe.2025.108635
Received 24 July 2025; Received in revised form 19 August 2025; Accepted 28 August 2025
Available online 1 September 2025
2214-7144/© 2025 Elsevier Ltd. All rights are reserved, including those for text and data mining, AI training, and similar technologies.

affinity, surface roughness and thickness of the active layer surface, and free volume which is associated with the crosslinking of the polymeric structure, have been mainly optimized for polymer membranes to yield both higher permeation and selective speciation performance [6]. Hydrophilicity is a key property to control the interactions of solutes with the surface of the membrane to either limit fouling or facilitate cleaning [7]. Both thickness and roughness of the selective layer have also been shown to affect permeation and fouling of the membrane materials. Smooth and thin surfaces minimize the flow resistance of the process water, whereas high operating pressures are required to overcome the flow resistance caused by the rough and thick surfaces thus leading to more fouling and cake formation [8,9]. Studies have proved that rise by a factor of a hundred in organic solvent permeance was obtained by reducing the thickness of the selective layer to sub 10 nm for NF thin film composite (TFC) membranes compared to commercial NF TFCs [10,11]. The cross-linking of the selective layer dictates the distribution of free volume across the macromolecular matrix which in turn controls rejection of solutes, ensuring an adequate level of permeance at the same time [12,13]. Such parameters must be better engineered to allow for the design of the next generation of molecular sieve membranes.

Nanoporous polymer membranes are commonly fabricated using phase inversion, electrospinning, and block copolymer self-assembly [14,15]. Phase inversion, particularly nonsolvent-induced phase separation (NIPS), offers scalability and tuneable porosity for UF and NF applications [16,17]. Electrospinning produces nanofiber mats with high surface area; post-treatments such as selective etching, phase separation, or thermal degradation introduce intra-fibre nano porosity, enabling fine-tuned membranes for filtration, sensing, and energy applications [18]. Block copolymer self-assembly enables highly ordered nanopore structures through microphase separation and selective domain removal, offering sub-20 nm pore control [19]. However, all these techniques involve with toxic organic solvents which are hazardous to living beings and environment [20]. Alternative green fabrication methods have been developed such as physical and chemical vapor deposition [15], phase transfer polycondensation [21], layer-by-layer assembly [22], plasma-enhanced polymerization (PP) or deposition [23,24].

Plasma polymerization offers a solvent-free, environmentally friendly method to create uniform, pinhole-free, and highly cross-linked coatings, enhancing membrane hydrophilicity, selectivity, and fouling resistance [25]. This fast, waste-free process improves surface properties while maintaining membrane integrity [26,27]. Plasma polymerization (PP) of 1H, 2H, 2H-perfluorodecyl acrylate (PFDA) on PDMS-coated PVDF membranes for membrane distillation (MD) applications increased surface roughness (497 nm to 525 nm) and imparted omniphobicity. High contact angles with water (144°), oil (124.4°), and ethanol/water (120.8°) confirmed resistance to both polar and nonpolar liquids [28]. The modified membranes showed excellent wetting resistance and stable PVMD performance with over 99.9 % salt rejection [29]. Another study utilized plasma polymerization and prepared plasma-induced polyacrylic acid-TiO_2 coated PVDF membranes [30]. The modification greatly improved membrane hydrophilicity, reducing the water contact angle from 83.5° to 9.1° and increasing water flux by four compared to conventional methods, while maintaining over 92 % oil rejection [31]. Acrylic acid was grafted via gas plasma-treatment onto electrospun PS/PAN nanofibrous foils, reducing the water contact angle to 0° and confirming enhanced surface hydrophilicity. The modified membranes achieved high separation performance, with fluxes up to 57,509 L m^{-2} h^{-1} for layered oil/water mixtures and 1390–6460 L m^{-2} h^{-1} for various oil-in-water emulsions [32,33]. Acrylic acid grafting, initiated by atmospheric pressure air plasma treatment, was used to modify polysulfone (PSf) UF membranes to enhance fouling resistance and optimize performance [34]. The PSf membranes with grafted PAA chains showed a 14 % increase in surface hydrophilicity, a 556 % rise in polar surface energy, and 26 % more negative zeta potential (at pH >6) compared to unmodified PSf. They also achieved full permeability recovery after water backwash, unlike native PSf, which recovered only 66–81 % [35]. These studies demonstrate that plasma-modified membranes, with their superhydrophilicity, high flux, and strong anti-fouling properties, are well-suited for wastewater treatment [36]. However, there is limited understanding of how the intrinsic properties of the selective layers such as chemical composition, crosslinking density, and surface energy affect overall membrane performance. Membrane-based separation technologies are vital for environmental restoration, going beyond water purification to rehabilitate degraded aquatic systems. By removing heavy metals, excess nutrients, persistent organics, and emerging pollutants like PFAS, membranes help restore ecological balance and protect biodiversity [37]. Their high selectivity, scalability, and low-energy operation suit treatment of industrial discharges, agricultural runoff, and contaminated groundwater. Advances in surface modification, such as plasma polymerization, allow tailoring for site-specific remediation, supporting sustainable restoration and safe water reuse [38].

While plasma polymerization has proven effective in tuning membrane surface chemistry, hydrophilicity, and fouling resistance, most studies focus on general performance enhancement without resolving *how* specific plasma modes influence contaminant rejection mechanisms. There is a lack of systematic understanding of how pulsed plasma versus continuous wave (CW) plasma polymerization affects the structure–property relationships of the selective layer, such as crosslinking density, surface energy, and free volume and how these, in turn, govern the rejection of persistent, small-molecule pollutants like PFAS. Addressing this gap, the present work fabricates ultra-tight, highly crosslinked ppAAc-coated PSf membranes using both pulsed and CW plasma modes and directly correlates plasma parameters with PFAS rejection mechanisms. By comparing these two plasma regimes, this study provides fundamental insights into tailoring selective layer architecture for improved removal of environmentally persistent contaminants, while maintaining a favourable balance between flux and selectivity.

To address this, the present study focused on fabricating uniform, highly cross-linked, semi-permeable films via plasma polymerization of acrylic acid (ppAAc) onto polysulfone (PSf) membranes. This modification introduced a selective barrier layer that reduced water permeance but significantly improved salt rejection. The study showed that plasma power and treatment duration significantly affected film properties such thickness and surface energy. These changes directly influenced membrane performance, enabling precise control over selectivity, permeability, and fouling resistance. The resulting ultra-tight membranes showed strong potential for removing large organic contaminants, offering a favourable balance between selectivity and throughput. Filtration tests using PFAS were used to estimate the molecular weight cut-off (MWCO), and membrane performance was further assessed through fouling resistance and recovery over multiple filtration cycles. At the same time, plasma-modified membranes demonstrated high effectiveness in removing PFAS compounds, particularly those with higher molecular weights, while maintaining higher flux compared to conventional nanofiltration (NF) and reverse osmosis (RO) membranes.

2. Materials and methods

2.1. Materials and chemicals

Flat sheet UF PSf membranes (MWCO 30, 000–50, 000, Pureach Tech Ltd., Beijing) were used as membrane substrates in this study for plasma polymer deposition. The monomer precursor used in the plasma polymerization was acrylic acid (AAc, anhydrous contains 200 ppm 4-methoxyphenol as an inhibitor, 99 %), were purchased from Sigma Aldrich. Inhibitor 4-methoxyphenol (MEHQ) was removed by filtering it through a column filled with alumina (purity, ≥98 % Al_2O_3 basis), which was also purchased from Sigma Aldrich. Sodium chloride (NaCl, ACS reagent, ≥99.0 % purity), and magnesium sulfate (anhydrous, ReagentPlus®, ≥99.5 % purity) were purchased from Sigma-Aldrich

(Australia).

Four PFAS substances, such as tridecafluorohexane-1-sulfonic acid potassium salt (≥98.0 %, PFHxS), heptadecafluorooctanesulfonic acid potassium salt (≥98.0 %, PFOS), perfluorononanoic acid (97 %, PFNA), and perfluorotetradecanoic acid (96 %, PFTeA) were purchased from Sigma-Aldrich for the PFAS rejection tests. The molecular weight corresponding to PFHxS, PFOS, PFNA, and PFTeA was 438 Da, 538 Da, 464 Da, and 714 Da, respectively. PFHxS, PFOS, PFNA, and PFTeA were selected as representative PFAS compounds because they span a range of chain lengths, functional groups, and hydrophobic–hydrophilic balances, allowing assessment of rejection performance across structurally diverse PFAS. PFHxS (C6, sulfonate) and PFOS (C8, sulfonate) represent short- to long-chain perfluoroalkyl sulfonates with high environmental persistence. PFNA (C9, carboxylate) and PFTeA (C14, carboxylate) represent long-chain perfluoroalkyl carboxylic acids with differing molecular sizes and polarity compared to sulfonates [1]. This diversity enables evaluation of how molecular size, functional group chemistry, and hydrophobicity influence rejection mechanisms in plasma-modified membranes, providing a robust model set for environmental relevance and mechanistic insight [1].

Target analytes and their isotope labeled analogs for the PFAS analytical testing were purchased from Wellington Laboratories (Guelph, Canada). All analytes were of >98 % chemical and isotopic purity. Methanol, Methyl-t-butyl ether (MTBE), glacial acetic acid, and ammonium acetate were purchased from Merck (Australia) and of either Liquid chromatography-mass spectrometry (LC-MS) grade or >99.9 % purity. Laboratory grade water used in the analysis was obtained from a Waters Milli-Q Water Purification unit (Milford, USA). Solid-Phase Extraction cartridges (Oasis 500 mg hydrophilic/lipophilic balance) were purchased from Waters (Milford, USA). Sample extracts were evaporated using a TurboVap LV concentration workstation purchased from Caliper Life Sciences (Hopkinton, USA) and cylindered ultra-high purity nitrogen (BOC, Australia).

2.2. Fabrication of the semi-permeable plasma polymerized thin films

Plasma polymerization was conducted using a custom-built, inductively coupled RF 13.56 MHz low-pressure plasma system. The procedures for plasma polymerization have been described previously [27]. Plasma can be generated in two power modes- continuous wave (CW) and pulsed (P)- by the CESAR® RF generator (Advanced Energy®, USA) through an antenna. The antenna comprises two copper wires looped around the left side of the glass cylinder, which is close to the gas and monomer inlets. A matching network (EJAT6, Kurt J. Lesker Co., USA) enabled a 100 % transfer of RF power into plasma. A PSf membrane (8 × 9 cm) was prepared for each plasma polymerization, located coaxially in the plasma chamber.

The plasma chamber was evacuated to $5.0 \times 10^{-2} \pm 0.2$ mbar and maintained at this pressure for 15–20 min using a rotary pump. All monomer solutions were degassed before introducing them to the chamber. The reactor pressure was maintained at 0.1 mbar for 5–10 min to ensure that the monomer was delivered at a constant rate before plasma polymerization. After the chamber became vacuumed again, the membrane samples were first activated and cleaned by argon (Ar) plasma (CW, 100 W, 1 min, $7.5 \times 10^{-2} \pm 0.2$ mbar). The AAc monomer precursor was then introduced to the plasma reactor as a vapor during plasma polymerization. The plasma power input plays a vital role in controlling the cross-linking structure of thin films and the density of primary chemical domains derived from monomers. Hence, the impacts of plasma conditions were studied by changing the power input for CW plasma polymerization, and average power input controlled by the duty cycle ($DC = t_{on}/(t_{on} + t_{off})$) under CW + P mode [39], respectively, over the same treatment duration. The average power equals to the peak power multiplying duty cycle [27].

2.3. Membranes surface and morphology characterization

The Scanning Electron Micrographs (SEMs) were acquired on a Supra 55VP FEG SEM (Zeiss, Oberkochen, Germany) with a 5-nm carbon films prior to imaging. The SEM images were taken at an accelerating voltage at 5 kV and a working distance of 5 mm. A Zeiss Secondary Electron detector under InLens mode was applied for acquiring SEM images with a higher surface resolution, enabling analysis of the surface properties of the plasma polymerized thin films, especially the number of pores. In addition to pore counting, graphical analysis of the acquired SEM images, such as estimation of film thickness, was completed by ImageJ (NIH, USA).

The cross-section of the pristine PSf and PSf deposited with plasma polymerized AAc films (ppAAc/PSf) composite membranes prepared at 50 W for 5 and 10 min under CW mode was analysed by transmission electron microscopy (TEM) to represent the growth of ppAAc films. The cross-section of the ppAAc/PSf composite membranes prepared at 100 W after 10 min deposition was also viewed by the TEM. The impact of plasma power input on the surface morphology and structure of the pristine PSf was studied by comparing the cross-section of the samples prepared at 50 and 100 W after 10 min plasma treatment. The cross-sectional TEM specimens were prepared by using Focus Ion Beam (FIB) in a dual-beam FIB-SEM (FEI Quanta 3D) following a previously reported procedure [40]. Prior to FIB milling, platinum (Pt) layers of ~1.5 μm thick were deposited under an electron beam operated at 5 kV, to protect the film from FIB damage. Thin slices of cross-sections were milled out using FIB operated at 30 kV. Then, the cross-section was lifted on to a TEM holder using a micro-manipulator. Finally, the specimens were thinned down to around 200 nm thick. At the final thinning stage, a low voltage of 2 kV was used to minimize the FIB damage. TEM observation was carried out using a JEOL 2100F FEG-TEM, operated at 200 kV. The images were taken in scanning-TEM mode (STEM) using an annular bright-field detector.

Atomic force microscopy (AFM) analysis was performed in tapping mode using a Cypher AFM (Asylum Research, Oxford Instruments). The samples were mounted onto magnetic support using double-sided tapes. The resonance frequency and spring constant of a cantilever are 150 kHz (±100 kHz) and 40 N/m, respectively. The actual resonance frequency was automated on Igor Pro 6.35A5 software, which is the same software for AFM images acquisition. The AFM images were acquired using a scan speed of 0.5 Hz and scan sizes of 1×1 μm^2 and subsequently processed by using Gwyddion 2.50. The tapping mode was selected for AFM analysis to avoid scratches to the plasma polymerized thin films and tip contamination through continuously contact the cantilever tips with soft, thin films polymer materials [41]. Water contact angle (WCA) analysis was conducted using a goniometer (Biolin Scientific). Triplicate measurements were performed by adding 4 μL of deionized water drops in three different spots across the surface of the samples. The contact angle data was recorded after 5 s since the droplet was in contact with the surface of relevant samples. OneAttension Theta Lite Software was used to fit the droplet images with the Young-Laplace equation and to obtain the final contact angle results.

The long-range surface roughness of the ppAAc/PSf composite membranes was measured before each PFAS rejection tests and after cleaning to study the degree of the adsorption of PFAS, using a laser microscope (Olympus, LEXT OLS4100). The surface profile with a scan size of 32×32 μm^2 was obtained at a pitch size of 0.01 μm. All profile images were taken using a 50× objective (∞/0/FN18) with further zooming in 8 times at the surface of relevant samples. LEXT software was used for LSM profile image acquisition and processing.

2.4. Chemical and surface charge characterization

Single-point attenuated total reflection-Fourier transform infrared (ATR-FTIR) spectroscopic analysis was performed using a bench-top single-reflection diamond ATR sampling module (Platinum ATR™)

with a deuterated triglycine sulphate (DTGS) detector (Bruker Optik GmbH, Ettlingen, Germany), to investigate the retention of the chemical functional groups for the composite membranes after plasma polymerization. The ATR-FTIR spectra were collected across 4000–600 cm^{-1} spectral range with a resolution of 4 cm^{-1} and 32 co-added using OPUS 8.0 software (Bruker).

The film homogeneity and the distribution of chemical domains of the plasma polymerized thin films were analyzed at a high-resolution using synchrotron-FTIR microspectroscopy at the Infrared Microspectroscopy (IRM) beamline, Australian Synchrotron (Clayton, Victoria). The IRM beamline was equipped with a Bruker Vertex 80v spectrometer coupled with a Hyperion 3000 FTIR microscope and a liquid nitrogen-cooled narrow-band mercury cadmium telluride (MCT) detector (Bruker Optik GmbH, Ettlingen, Germany). All the synchrotron-FTIR spectra were recorded within a spectral range of 3900–750 cm^{-1} using 4-cm^{-1} spectral resolution. Blackman-Harris 3-Term apodization, Mertz phase correction, and zero-filling factor of 2 were set as default acquisition parameters using OPUS 8.0 software suite (Bruker).

In particular, the plasma polymerized films were mapped using an in-house developed macro ATR-FTIR device equipped with a 250-μm-diameter facet germanium (Ge) ATR crystal ($n_{Ge} = 4.0$), and a 20× IR objective (NA = 0.60; Bruker Optik GmbH, Ettlingen, Germany) [42]. The unique combination of the high refractive index property of the Ge ATR crystal and the high numerical aperture (NA) objective used in this device, when coupled to the synchrotron-IR beam, allows surface characterization of the membrane films to be performed without scattering artifacts and at higher spatial resolutions than those achievable in transmission and reflectance modes. The high-resolution synchrotron macro-ATR-FTIR maps were acquired with a projected aperture of 3 μm at 0.5 μm step size, using 32 co-added scans to cover 20 × 20 $μm^2$ area on the film. Chemical maps were produced based on integrated areas under the domain functional groups (i.e. carbonyl stretching vibration) and corresponding average spectra were extracted from each map using OPUS 8.0 software (Bruker). These chemical maps revealed the distribution of the carbonyl groups inherited from the acrylic acid monomer precursors across the surface of the membrane film.

X-ray Photoelectron Spectroscopy (XPS) linescans were acquired by a K-alpha X-ray photoelectron spectrometer (Thermo Fisher Scientific, Massachusetts, United States), at the Micro Nano Research Facility (MNRF), RMIT University. The quantitative elemental composition of the pristine PSf and the PSf deposited with PPTF samples was provided for a surface depth of 1–5 nm. An Al Kα (1486.6 eV) X-ray source was used as the excitation source, and the anode was maintained at 250 W, 10 kV, and 27 mA at a chamber pressure of 1×10^{-9} Pa with a beam spot size of 400 μm × 400 μm. Elemental spectra were analyzed using CasaXPS software, and the deconvolution of the high-resolution spectra was based on the Shirley method. The spectra were calibrated using the C1s peak of adventitious carbon at 284.6 eV.

An Electro Kinetic Analyzer (Surpass Anton Paar) was used to measure the surface charge of the pristine PSf and PSf deposited with plasma polymerized thin films. Two membrane coupons were molded onto two 20 × 10 mm cells, respectively, which were later positioned face-to-face in the analyzer. The gap between membrane coupons creates the streaming channel. The streaming channel was adjusted to approximately 0.1 mm to generate a pressure difference from 600 to 200 mbar for the streaming potential measurement. The potassium chloride (KCl) solution at a concentration of 1 mM was first cycled through the analyzer, and then 0.1 M HCl or NaOH was doped to adjust pH for streaming potential measurements. Quadruplicate zeta potential measurements were obtained in a range of pH values varied from 4 to 9.

2.5. Filtration and desalination tests

The DI water permeance and salt rejection of pristine PSf and PSf deposited with plasma polymerized thin films were conducted using crossflow filtration units (HP4750 and CF042, Sterlitech Corp., WA, USA). Two solutions, including 2000 ppm NaCl and 4000 ppm $MgSO_4$ were prepared for the desalination filtration. The DI water permeance of all tested membrane samples was recorded after 2 h compaction at 5 bar. The DI water feed was replaced by NaCl and $MgSO_4$ solutions for the salt rejection tests, respectively. The filtration system recycled the salt solution for 1–2 h before measuring the conductivity of the permeate. The conductivities of the salt feed and permeate were measured using an electrical conductivity meter (TPS, WP-81, Queensland, Australia). The DI water permeance and salt rejection were calculated using Eq. (1).

$$f = V/A \times t \times P \tag{1}$$

where f is the permeance, V is permeate volume (L), A is effective membrane area (m^2), t is time over which volume V was collected (h), and P is the feed pressure applied during the filtration tests [26,43] as per Eq. (2).

$$SR\% = 1 - (C_p - C_f) \times 100\% \tag{2}$$

where SR% is the salt rejection, C_p and C_f are the conductivity (μS/cm) of salt concentration in the permeate and feed, respectively [26,43].

For the PFAS rejection test, all tested membrane samples underwent DI water compaction at 6 bar until steady permeance was reached. The water permeances (f_1) were further monitored for another 2 to 4 h at 5 bar. The permeance of all tested membranes was measured at 5, 10, 20, and 30 h (f_P) after the experiment began. The conductivity of the aqueous solutions collected from feed and permeate was recorded for estimating the quantities of PFAS substances. The concentration of PFAS materials in feed and permeate collected from each rejection test were also analyzed by LC-MS/MS through the direct injection PFAS method developed at UNSW, Australia. The crossflow filtration units were cleaned by ethanol and rinsed with DI water after each PFAS rejection test. Membrane samples were put back into the system for 2 h of DI water crossflow rinsing without applying any pressure to the membrane samples. The water permeance was monitored again for another 4 h (f_2) [44].

2.6. Water analysis for perfluoroalkyl substances

An analytical method for the determination of 22 perfluoroalkyl substances (PFAS) in water was developed using a solid-phase extraction (SPE) sample preparation and the cleanup step followed by separation by ultra-high performance liquid chromatography and identification and quantification by tandem mass spectrometry (UHPLC-MSMS). Isotope dilution was employed to quantify target analytes with reporting limits of 5–20 ng/L. Working stock solutions of individual target analytes and isotope labeled internal standards (ISTDs) were prepared in methanol and stored refrigerated (4 °C). These working stocks of ISTDs and mixed analytes were prepared in 60 % methanol in water and used to prepare calibration series and spiked samples.

3. Results and discussion

In the following sections, the physical, structural and chemical properties of the plasma modified membranes will be presented to investigate the morphology and intimate interfacing between the active layer and polymeric membrane. The sections further investigate the impact of the homogeneous film structure on membrane performance, including PFAS rejection, long-term permeance stability, and the effects of solution chemistry on permeance.

3.1. Membranes surface and morphology

The porous structure of the pristine PSf membranes Fig. 1(a) was gradually covered by the deposition of the ppAAc films as a function of the plasma polymerization duration (Fig. 1(b-d). However, a few pinholes appeared at the surface of the ppAAc films, highlighted by red

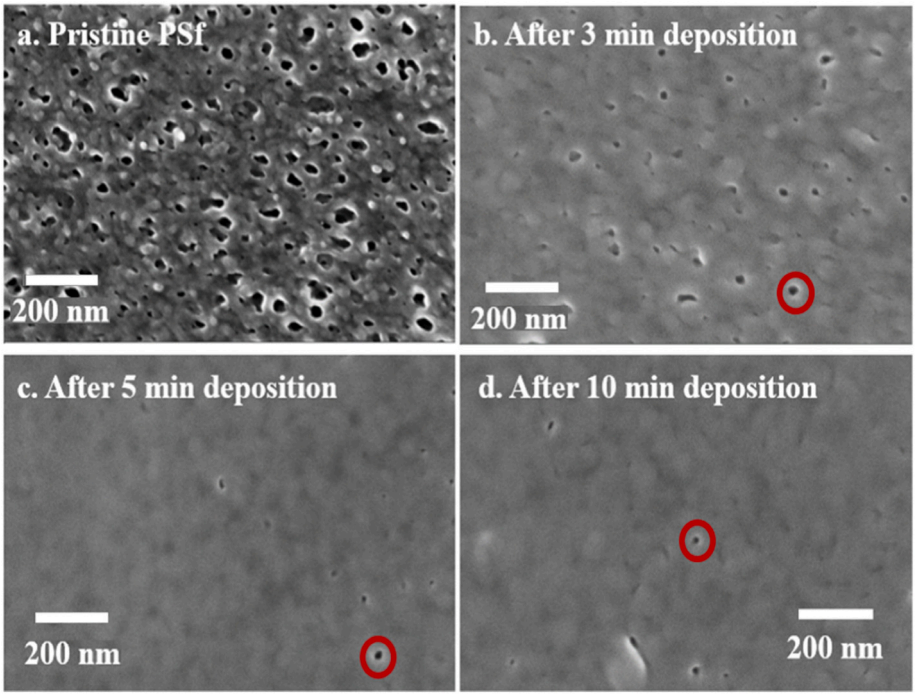

Fig. 1. The SEM images of the (a) pristine PSf control, and the PSf deposited with plasma polymerized acrylic acid (ppAAc) films prepared at 50 W and 0.1 mbar (reactor pressure) for (b) 3 min, (c) 5 min, (d) 10 min at high magnification.

circles in Fig. 1(b-d). Similar morphology was reported previously, explaining that the pinholes, also known as interstitial spaces, were a result of the increasing internal stress generated by the growth of the polymer films [45,46]. The ppAAc prepared at 100 W for 3, 5, and 10 min showed similar morphology, as given in the supplementary information as Fig. S1.

The growth kinetics of plasma-polymerized films show a cyclical deposition pattern on the surface of silicon wafers, with changes occurring on a per-second timescale. This behavior suggests that film formation is influenced by time-dependent plasma dynamics, including fluctuations in reactive species density, surface activation, and energy input [46]. Based on the growth behavior, the porous PSf substrates were gradually covered by clusters of polymer nodules, as shown in Fig. 2(a). These activated polymer particles settled on both the bare PSf surface and the already-deposited ppAAc film, helping to fill gaps and smooth the surface. This led to the formation of a more continuous and uniform film layer, as seen in Fig. 2(b).

The thickness of the plasma polymerized films built up as the growth cycle continued Fig. 2(c). The ppAAc films were expected to exhibit a structure like that illustrated in Fig. 2(d), characterized by a

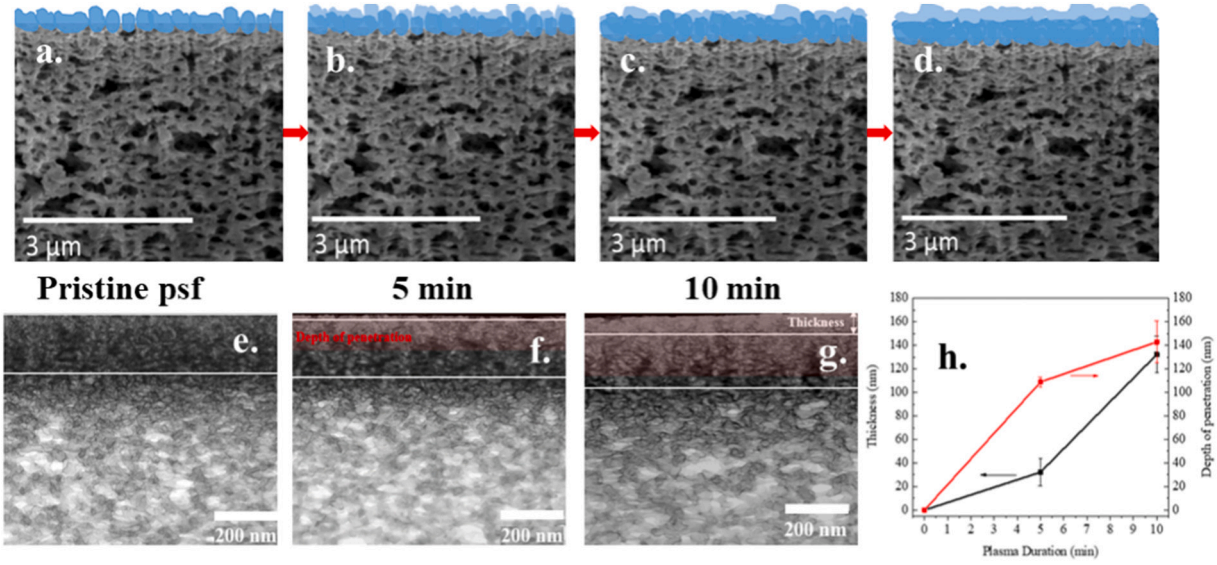

Fig. 2. Schematic representing the growth kinetics of ppAAc (a) formation of many islands consisting of aggregated polymer nodules, (b) activated radical-transferred polymer nodules settled on both bare PSf and ppAAc-coated regions, (c) built up of the polymerized layer of AAc, (d) formation of homogeneous ppAAc active layer on the PSf surface. TEM images of the cross-section of the (e) pristine PSf, ppAAc prepared at 50 W and 0.1 mbar (reactor pressure) after (f) 5 min, (g) 10 min deposition, (h) thickness of the ppAAc films and depth of penetration of plasma polymerized materials were estimated based on the pixel intensity using ImageJ. The given scale bar applied to all TEM images listed here.

homogeneous layer formed on the PSf surface. The thickness of this layer varied depending on the plasma treatment duration, with longer exposure times resulting in increased film thickness due to continued deposition and polymer growth.

The cross-sectional TEM images of both the pristine PSf control and the ppAAc-treated samples Fig. 2(e-g) provided strong evidence supporting the film growth kinetics. In the pristine PSf membranes, a gradient in material density was observed based on image brightness and contrast, with higher polymer density evident at the outermost surface. This gradient intensified further beneath the surface, as indicated by a reduction in electron transmittance, seen in the region highlighted between two white lines in Fig. 2(e-g). The height above the top white line corresponds to the thickness of the ppAAc films deposited on the PSf surface. This thickness increased significantly from 32.3 ± 11.7 nm to 132.2 ± 15.6 nm, when the plasma deposition duration was extended from 5 to 10 min, clearly indicating non-linear time dependent film growth Fig. 2(h). In the early phase, film growth was slow due to isolated nodule formation, but it accelerated as these merged and surface reactivity increased. Over time, reduced etching and stable deposition further enhanced the growth rate.

Additionally, the TEM images revealed a notable increase in brightness beneath the PSf surface following plasma treatment, suggesting that ppAAc material not only formed a surface layer but also infiltrated the porous PSf matrix [47,48]. After 10 min of deposition, the ppAAc was found to have penetrated to a depth of 142.9 ± 17.9 nm (analyzed on ImageJ), which is approximately 16.1 to 51.8 nm deeper than the penetration observed after 5 min of treatment, accounting for variability Fig. 2(h). These findings strongly suggest that prolonged plasma exposure facilitates greater incorporation of ppAAc material into the PSf structure, both at and below the surface.

Surface morphology changes, particularly in roughness, were analyzed through AFM images provided in supplementary information in Figs. S2 and S3. The deposition of the ppAAc films induced a smoothing effect on the pristine PSf membranes, as quantified in Fig. 3 (a). The difference in the roughness of the ppAAc prepared at 50 and 100 W for the different duration was less than 1 nm, suggesting that the ppAAc films were morphologically homogeneous over a 1 × 1 μm AFM scan. The surface of the ppAAc prepared at 100 W was slightly smoother, with a difference between 0.38 and 0.89 nm, compared to the films prepared at 50 W for 5 and 10 min, respectively. High plasma energy input induces a high degree fragmentation of the monomer precursors and simultaneously increases the intensity of the plasma bombardment at the surfaces of the pristine PSf or ppAAc films later based on proposed plasma polymerization mechanisms [49,50]. Therefore, highly cross-linked surfaces composed of small fragments attributed to smoother surfaces [51].

Furthermore, increased hydrophilicity was observed on the PSf surface after ppAAc film deposition, with maximum water contact angle reductions of 81.1 % and 84.8 % observed for films subjected to 3 min of plasma treatment at 50 W and 100 W, respectively, compared to the pristine PSf (73.3 ± 2°), as represented in Fig. 3(b). The ppAAc films became less hydrophilic as the WCA rose up again by 2.8° and 10.6° for the films deposited at 50 and 100 W after 10 min deposition, respectively. The WCA results indicated that a higher degree of cross-linking occurred at 100 W after 10 min of treatment, leading to a surface with fewer hydrophilic functional groups generated by plasma polymerization of AAc. The observed increase in water contact angle after 10 min plasma deposition likely stems from multiple overlapping effects. Plasma treatment followed by acrylic acid deposition may remove surface polar fragments and low-molecular-weight species, leaving behind a denser and more hydrophobic coating layer [52]. High-energy and prolonged plasma exposure can further etch and smooth the film, exposing underlying hydrophobic substrates and diminishing the roughness-induced wetting enhancement [52]. Additionally, over time, hydrophilicity may decay as polar functional groups reorient or rearrange within the surface layer, leading to a modest increase in WCA [53].

3.2. Surface chemistry and chemical homogeneity

The impact of plasma treatment on surface chemistry and homogeneity was investigated using synchrotron-FTIR microspectroscopy, conventional bench-top ATR-FTIR, and XPS. Synchrotron-FTIR chemical mapping enabled a detailed spatial assessment of chemical distribution across the ppAAc-coated PSf surfaces.

Synchrotron-FTIR chemical maps, generated by normalizing spectra in the range of 1620–1530 cm^{-1} and integrating over 1750–1690 cm^{-1} for ν(C=O) carbonyl stretching mode, are shown in Fig. 4(a–c) for 50 W plasma treatments and Fig. 4(e–g) for 100 W plasma treatments, across durations from 3 to 10 min. The corresponding maps of pristine PSf are included in Fig. S4. At 50 W, the absorption intensity of the ν(C=O) bond increased progressively with treatment time, indicating enhanced surface functionalization. This trend was corroborated by the bench-top ATR-FTIR spectra in Fig. 4d, which showed a gradual increase in the broad ν(C=O) absorption centered at ~1720 cm^{-1}, attributed to the ν(C=O) stretching modes of carboxylic acids (typically around 1710–1720 cm^{-1} in the ppAAc samples). These spectra clearly indicated that the concentration of –COOH groups increased with plasma treatment duration, as reflected by a continuous rise in the intensity of the –C=O band. As the plasma treatment time was extended, the carbonyl

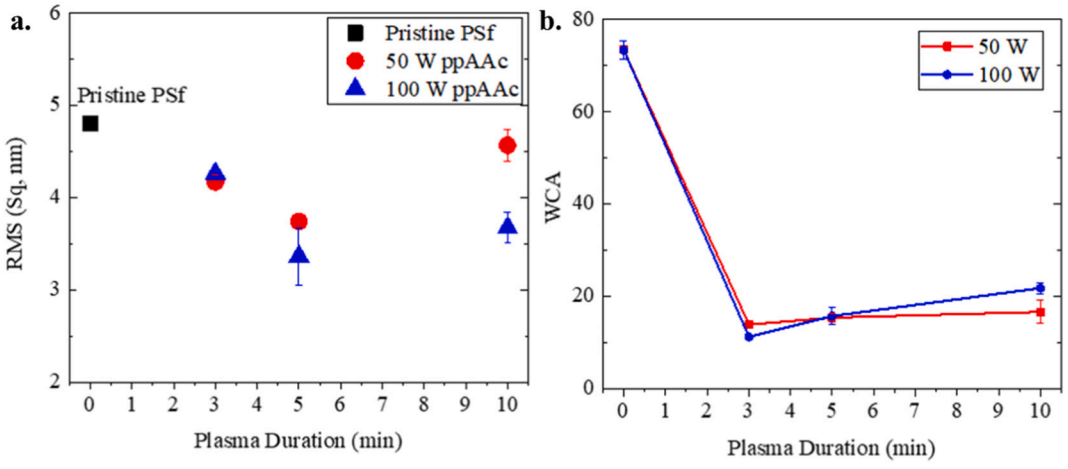

Fig. 3. (a) The root-mean-square (RMS) roughness, (b) and water contact angle (WCA) of the ppAAc films prepared at 50 and 100 W for different durations (3, 5, and 10 min).

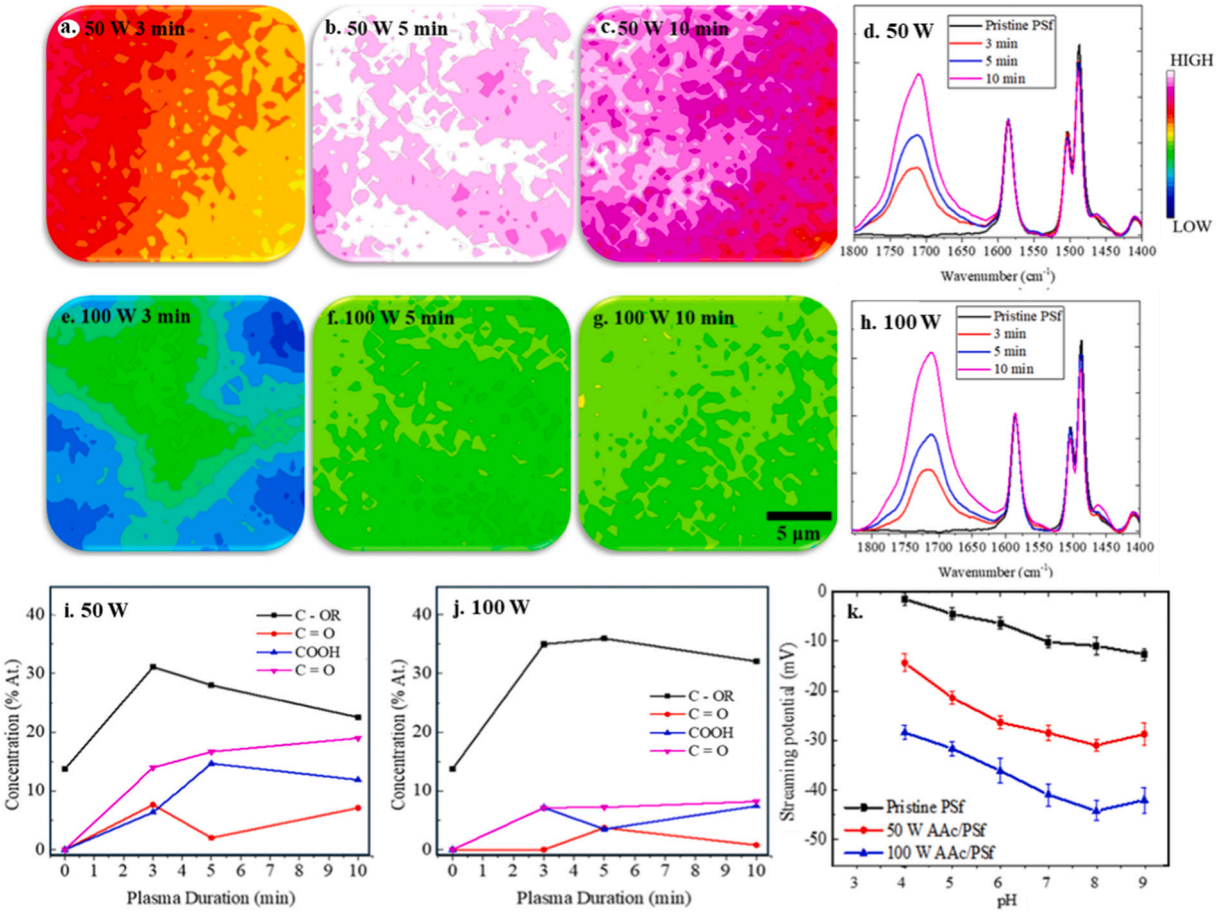

Fig. 4. Synchrotron-FTIR chemical maps of carbonyl groups based on integrated areas under the ν(C=O) stretching vibration (1750–1690 cm^{-1}) of the PSf deposited with ppAAc films prepared using (a-c) 50 W and (e-g) 100 W at 0.1 mbar (reactor pressure) for (a, e) 3 min, (b, f) 5 min, and (c, g) 10 min. Note that the range of intensity scale was set the same for all chemical maps from 0 to 20 for comparison purposes. (d, h) Representative bench-top ATR-FTIR spectra of pristine PSf and ppAAc PSf samples. (i-j) XPS analysis showing the concentrations of C-OR, C═O and COOH, as a function of plasma duration observed using 50 W and 100 W, respectively. (k) Streaming potential of pristine and the ppAAc films prepared at 50 and 100 W for 10 min.

content increased, which was consistent with the observations from TEM cross-sectional images and other related studies [54,55].

A similar pattern was observed for the 100 W treated samples in Fig. 4(e–g) and h. Although the increase in carbonyl group concentration was more subtle than those at 50 W, a uniform concentration of the carbonyl groups was shown across the surface from 5 min of plasma exposure. Quantitatively, ppAAc films treated at 50 W exhibited 1.2–1.7 times higher absorption intensities than those treated at 100 W, suggesting that lower plasma power may enhance the formation of surface functional groups. This is likely due to reduced aggressive etching or milder plasma exposure, preserving functional group integrity. Conversely, higher plasma power can lead to excessive fragmentation and cross-linking, reducing the availability of functional groups — a phenomenon well explained by the fragmentation model of plasma polymerization [49,50]. In this fragmentation model, high plasma power leads to deeper monomer fragmentation, forming highly cross-linked structures with fewer original functional moieties. Lower power, on the other hand, tends to produce less fragmentation and more linear polymers with retained chemical functionality. The process mechanisms of plasma polymerization could also be attributed to the variation of the carbonyl contents being produced. Constant competition between the deposition and plasma ablation at the outmost surface could cause the variation in surface chemistry [49,50].

XPS analysis was used to assess the surface chemistry of pristine PSf after ppAAc deposition, evaluating the concentration of functional groups from plasma polymerization. The changes in functional group concentration at different plasma treatment times are presented in Fig. 4 (i-j) for 50 W and 100 W treatments, respectively, confirming the chemical trends observed by the FTIR technique. At 50 W, carbonyl-related species (–C–OR, C═O, and –COOH) increased substantially after just 3 min of plasma exposure. While the concentrations of C═O and –COOH did not increase linearly, the total carbonyl content increased from 13.9 to 18.9 % at.% between 3 and 10 min. The gradual decrease in –C–OR concentration from 31.1 to 22.5 at.% as time increased from 3 to 10 min suggested increased cross-linking in the ppAAc films. Similarly, at 100 W, the carbonyl-related groups increased from 0 to 7.1 % at.% after 3 min of plasma treatment and further increased to 8.2 % at.% after 10 min. However, at 100 W, the –C–OR concentration remained relatively stable (32–35 % at.%) for various plasma durations. This slower increase in the formation of carbonyl functional groups at 100 W supports that plasma power has a stronger influence than treatment time on the final surface chemistry [56].

Synchrotron-FTIR and XPS analysis together confirmed that ppAAc films achieved good chemical homogeneity after >3 min of plasma treatment at both power levels. However, 50 W was more effective at preserving carbonyl functional groups during extended treatment, while 100 W led to greater cross-linking and loss of functional contents even though the films remained microscopically homogeneous. In particular, the XPS results matched synchrotron chemical maps, showing that the ppAAc structure became highly cross-linked with fewer carbonyl groups as plasma power increased. These findings align with previous studies using different monomers (e.g., methylcyclohexane, ethylcyclohexane),

where higher plasma energy led to greater fragmentation and lower functional group retention [50,57,58]. Higher plasma power input also introduced more highly energetic plasma particles to enhance the plasma ablation, attributing the variation in the surface chemistry of ppAAc films [50,54].

In addition, data from streaming potential measurements in Fig. 4(k) revealed that the pristine PSf membranes carried a weak negative surface charge (−11 ± 2 mV at pH 8). In contrast, the surface of the ppAAc/PSf samples after plasma treatment became more negatively charged, indicating a shift towards the alkaline pH range. Furthermore, the surfaces of the ppAAc films prepared at 100 W for 10 min exhibited a strong negative charge, with a streaming potential of −44 ± 2 mV at pH 8, which was more negatively charged than the samples prepared at 50 W, which had a streaming potential of −31 ± 2 mV at pH 8. As supported by the XPS results, the ppAAc films prepared at 100 W retain more ionizable functional groups such as ether (–C–OR) and hydroxyl groups, which is attributed to either plasma-induced polymerization of AAc or chemical rearrangement at high power input. These groups can deprotonate in water, making the surface more negatively charged. This is likely due to plasma-induced polymerization or chemical rearrangement at higher power.

3.3. Pure water and salts rejection tests

The cross-linking degree was further assessed by testing the ppAAc-deposited PSf in crossflow filtration units, focusing on DI water permeance and salt rejection to explore the relationship between surface properties and membrane performance.

It was observed that the DI water permeance of the ppAAc deposited PSf dropped by 14.5 %, 68.7 %, and 87.2 % after 3-, 5-, and 10-min plasma treatment at 50 W from 198.3 ± 5.8 L. m^{-1}. h^{-1}.bar^{-1} (pristine PSf control), respectively, as shown in Fig. 5(a). Meanwhile, the PSf deposited with the ppAAc films prepared at 100 W, also experienced losses in DI water permeance by 64.6 %, 74.3 %, and 87.5 % after 3-, 5-, and 10-min plasma polymerization, respectively, compared to the pristine PSf control, represented in Fig. 5(a). The results showed a strong correlation between membrane performance and the thickness of the ppAAc films. As shown in the TEM images in Fig. 2(e–g), increasing the ppAAc thickness through plasma treatment enhanced the effectiveness of the membrane as a diffusion barrier against DI water molecules. The salt rejection performance was inversely proportionally related to the DI water permeance. The NaCl rejection gradually increased from 2.94 ± 0.4 % (pristine PSf control) to 3.8 ± 0.7 %, 6.5 ± 0.5 %, and 7.9 ± 0.2 % after 3-, 5-, and 10-min deposition at 50 W, respectively, demonstrated in Fig. 5(a). Similarly, the ppAAc films prepared at 50 W showed improved ability to reject $MgSO_4$ salts, with the highest rejection reaching at 11.3 ± 0.9 % for 10 min plasma treated membrane Fig. 5(a). The higher rejection rate for $MgSO_4$ compared to NaCl was expected because size exclusion was the main factor affecting the movement of hydrated ions [59]. A similar trend of NaCl and $MgSO_4$ rejection was observed for the PSf membrane treated with ppAAc prepared at 100 W, as shown in Fig. 5(b). However, the salt rejection of the ppAAc films prepared at 100 W against either NaCl or $MgSO_4$ was higher than that of the ppAAc films prepared at 50 W, respectively. Especially, the rejection against $MgSO_4$ was enhanced by 1.5–2 times by increasing power from 50 to 100 W. The DI water permeance was in accordance with the salt rejection performance, as the DI water permeance of the ppAAc films prepared at 100 W was lower than that prepared at 50 W by 1–2.5 times. Both salt rejection and DI permeance performance supported that the highly cross-linked structure with less free interfacial spaces between

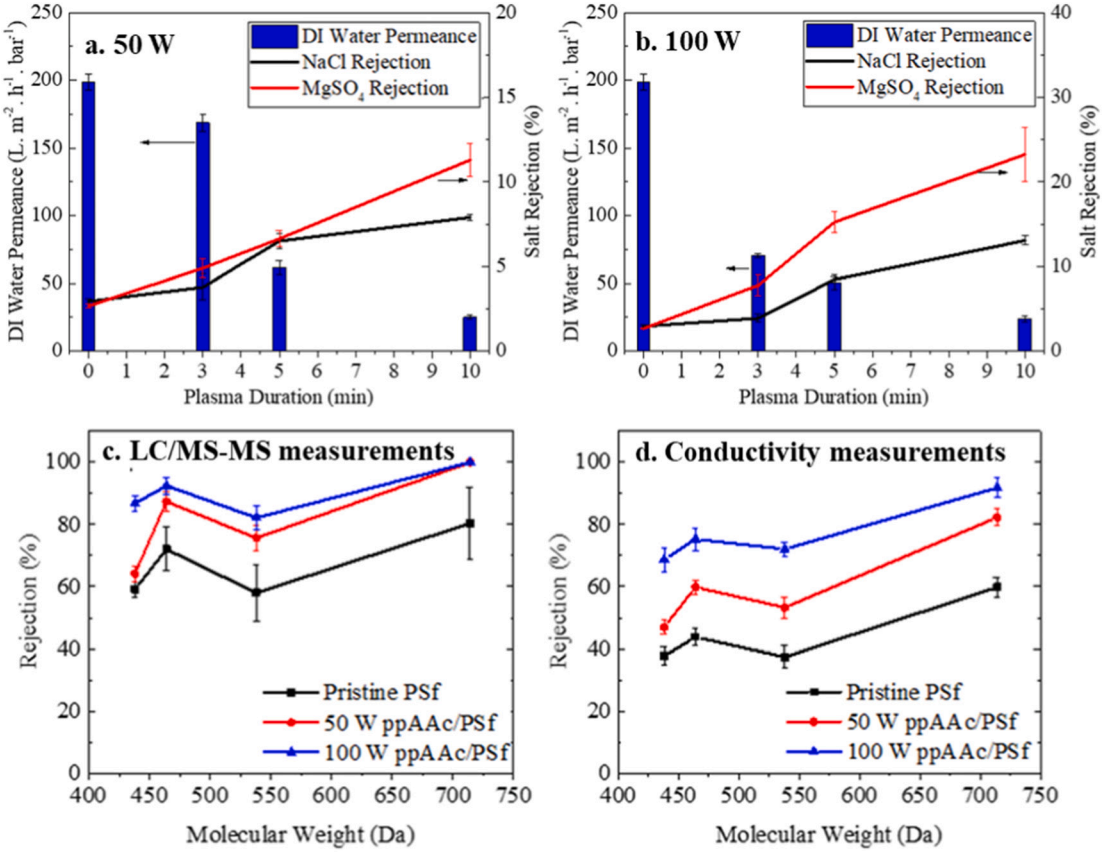

Fig. 5. The DI water permeance of the pristine PSf, with the ppAAc produced from plasma duration series at (a) 50 and (b) 100 W in crossflow test conditions: 5 bar inlet pressure at 20 °C. The rejection rate of PFAS substances by pristine PSf, the ppAAc/PSf composite membranes prepared at 50 and 100 W estimated based on (c) LC/MS-MS and (d) conductivity measurements.

chemical bonds was formed at the higher plasma input. In line with the solution diffusion theory, a highly cross-linked structure with less interfacial free spaces hinders the diffusion of water molecules and hydrated salt ions, and vice versa [60,61].

The ppAAc films prepared at 100 W for 10 min provided the optimum filtration performance in this case study, rejecting 13.07 ± 0.53 % of NaCl and 23.25 ± 3.19 % of $MgSO_4$, and providing 23.99 ± 2.19 L.m^{-1}.h^{-1}.bar^{-1}. However, the product of the ppAAc – deposited PSf can be categorized as tight ultrafiltration membrane after comparing its NaCl rejection with the commercial RO and NF membranes (BW30–400 and NF270, FILMTEC™) which can achieve 99.5 ± 0.5 % [62] and 56.07 ± 0.55 % (measured in this study), respectively.

3.4. PFAS rejection performance

In addition to their effectiveness in salt rejection, the ppAAc-deposited PSf membraces were also evaluated for their ability to remove PFAS from water. The chemical formula and molecular weight of PFHxS, PFOS, PFNA, and PFTeA used in this study is given in supplememtary information in Fig. S5 and conductivity curves against the concentration of the PFHxS, PFNA, and PFTeA are given in Fig. S6.

The pristine PSf membranes were able to reject 59.1 ± 2.5 % of PFHxS, 72.0 ± 7.0 % of PFOS, 58.0 ± 9.0 % of PFNA, and 80.4 ± 11.7 % of PFTeA, as shown in Fig. 5(c). The low efficiency of pristine PSf membranes in rejecting PFAS substances is largely due to the relatively large pore size on the order of 30 nm and the open porous structure of the pristine PSf materials generated by the phase inversion process. The deposition of ppAAc films via plasma polymerization enhances the selectivity for the ppAAc/PSf composite membranes. Such an improvement in selectivity also increases the rejection of PFAS substances. For ppAAc/PSf composite membranes prepared at 50 W, the rejection performance was 64.2 ± 2.5 % (+5.1) for PFHxS, 75.7 ± 4.1 % (+17.7) for PFOS, 87.4 ± 3.1 % (+15.4) for PFNA, 100 % (+19.6) for PFTeA, respectively. While for the composite membranes prepared at 100 W, the rejection performance was 86.8 ± 2.6 % (+27.6) for PFHxS, 82.2 ± 3.7 % (+24.1) for PFOS, 92.5 ± 2.8 % (+20.5) for PFNA, 100 % (+19.6) for PFTeA, respectively Fig. 5(c). Since the rejection performance of pristine PSf and ppAAc/PSf membranes for PFNA (464 Da) was slightly better than that for PFOS (538 Da), it is likely that rejection is governed by a mixture of size exclusion and hydrophobic/electrostatic interactions [63]. Indeed, perfluoro-sulfonic acids with the sulfonic group are intrinsically more hydrophobic than the perfluoro-carboxylic acids that contain carboxyl groups, but yet both offer a high density of electronegative groups, supporting direct electrostatic repulsion [64]. A combined QCM-D experiments, AFM, and molecular dynamics to study PFAS adsorption on a hydrophobic SAM surface was conducted recently [65]. It was observed that PFNA exhibited approximately twice the adsorption of PFOS even though both share the same fluorocarbon chain length because of stronger tail-insertion into the hydrophobic surface. PFNA's carboxylate head allowed deeper embedding of the hydrophobic tail, reinforcing adsorption [65].

Furthermore, the PFAS rejection rate calculated based on conductivity measurement showed a similar trend to that obtained from LC/MS-MS analysis Fig. 5(d). However, the rejection rate based on conductivity reading (Fig. 5(d)) was approximately 10–20 % lower at each data point than that based on LC/MS-MS analysis (Fig. 5(c)). The LC/MS-MS method was therefore considered more accurate to report the exact quantity of PFAS present in the solution, but the conductivity measurement can be considered as a more convenient and quicker on-site monitoring approach for single PFAS concentration assessment (>1 ppm) [66].

It was concluded that the higher the plasma power input, the more significant the improvement in rejection performance, suggesting that the formation of highly cross-linked structures improves the selectivity of the ppAAc films for PFAS rejection. The MWCO of the ppAAc/PSf composite membranes, defined for a rejection level over 90 % of the dissolved solutes by the tested membranes, was also extrapolated from these results [67]. The rejection results suggested that the MWCO of the ppAAc/PSf membranes prepared at 50 W was close to 600–700 Da since the rejection rate was close to 90 % for filtrating PFNA (464 Da) and PFOS (538 Da), while the rejection of PFTeA (714 Da) reached 100 %. Based on the same rationale, the MWCO of the composite membranes prepared at 100 W was found close to 500–600 Da.

3.5. Long term permeance performance assessment

The impact of plasma polymer material properties on permeance performance was evaluated to understand how variations in material characteristics influence membrane efficiency and stability over time. The normalized permeance of pristine PSf and ppAAc/PSf composite membranes over 30 h of PFAS filtration and after cleaning (after 36 h), under constant pressure at 5 bar, is shown in Fig. 6. The pristine PSf membranes exhibited a 19.7 % decrease in normalized permeance, dropping from 87.7 ± 3.5 L.m^{-2}.h^{-1}.bar^{-1} (after compaction) to 70.4 ± 4.3 L.m^{-2}.h^{-1}.bar^{-1} when filtering the smallest PFHxS (438 Da) molecules after 30 h of filtration, illustrated in Fig. 6(a). Over the same period of filtration, the ppAAc/PSf membranes prepared at 50 and 100 W experienced 9.8 and 4.8 % permeance reduction compared to their initial permeance of 52.1 ± 1.7 and 27.4 ± 1.4 L.m^{-2}.h^{-1}.bar^{-1}, respectively (Fig. 6(a)). A more significant decline in permeance for PSf membranes suggested that without plasma polymer coatings, the membranes were severely fouled due to the adsorption of PFHxS [68]. In contrast, a low degree in permeance reduction for the ppAAc/PSf composite membranes suggested a better fouling resistance against PFHxS. The composite membranes prepared at 100 W exhibited the lowest permeance reduction and hence the highest fouling resistance against PFHxS. A similar permeance reduction trend was obtained for pristine PSf and ppAAc/PSf composite membranes when filtrating PFNA, PFOS, and PFTeA, as represented in Fig. 6(b), (c) and (d), respectively.

Although the PSf membranes without plasma polymer coatings can deliver higher permeance, it offered a higher degree of hydrodynamic permeance drag [69] and hence experienced a higher degree of PFHxS adsorption. Electrostatic and hydrophobic interactions controlled surface adsorption mechanisms of PFAS, even in different systems such as mineral surfaces [70] and carbon fibers [64]. The pristine PSf encountered a higher degree of PFAS adsorption due to the affinity of the hydrophobic and anionic PFAS materials with less hydrophilic and negatively charged surfaces. In contrast, the ppAAc/PSf membranes with more hydrophilic and negatively charged surfaces, as highlighted in Table S2 were less sensitive to PFAS surface adsorption.

The permeance reduction for the PSf and ppAAc/PSf composite membranes was significant after 5 h of filtration, as illustrated in Fig. 6. Taken the filtration results against PFHxS as an example again, the normalized permeance was dropped by 14 % for the PSf membranes, but only 6 % and 4 % for the ppAAc/PSf membranes prepared at 50 and 100 W after 5 h. The normalized permeance difference after 5 and 30 h of filtrations was 5 % for the PSf membranes, 4 % and 0.3 % for the ppAAc/PSf membranes prepared at 50 and 100 W. This permeance reduction trend suggested that PFHxS adsorption primarily occurred during the first 5 h of filtration and that the passage of water molecules was subsequently hindered beyond this point. A similar gentle permeance reduction trend was reported for three commercial NF membranes (NF270, NF90, and DK) due to the adsorption of PFOS molecules throughout the filtration experiments for 96 h against 10 ppm PFOS solution at 14 bar [69].

Additional discussion on the impact of solution chemistry on permeance performance is provided in Section S1 of the Supplementary Information. These discussions further support that membrane permeance is significantly influenced by both the molecular weight of PFAS compounds and the surface properties of the membranes. The ppAAc/PSf membrane prepared at 100 W for 10 min demonstrated best

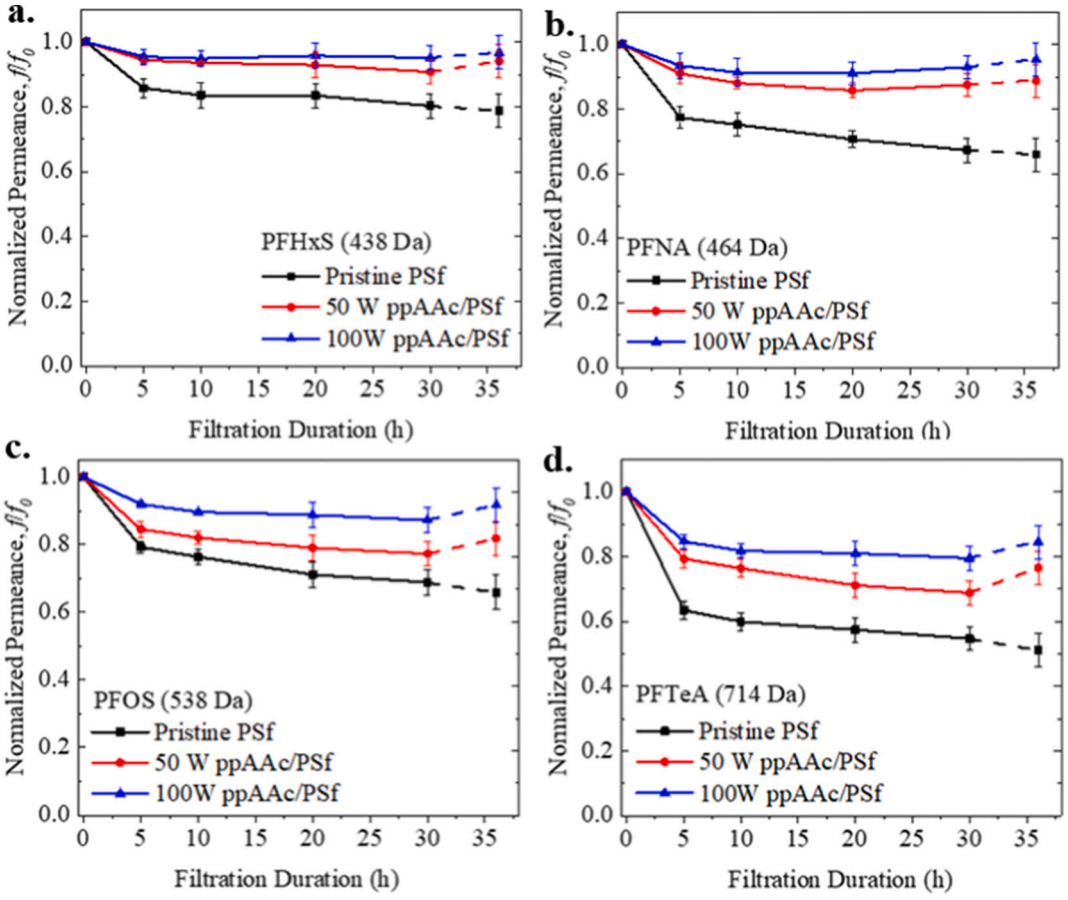

Fig. 6. The normalized permeance of the PSf without plasma coatings and ppAAc/PSf composite membranes prepared at 50 and 100 W throughout 30 h filtration and after DI water cleaning for (a) PFHxS, (b) PFOS, (c) PFNA, (d) PFTeA.

resistance to fouling, especially when challenged with larger PFAS molecules such as PFTeA. This highlights its enhanced stability and effectiveness in long-term filtration applications, particularly under conditions involving high-molecular-weight contaminants.

3.6. Comparison with literature

Plasma surface modifications substantially enhance membrane performance across ultrafiltration (UF), forward osmosis (FO), nanofiltration (NF), and reverse osmosis (RO) applications by altering surface chemistry and morphology. The membrane performance achieved in this study is compared with relevant literature and summarized in Table 1. For instance, Ar/O_2 plasma treatment on polysulfone (PSF) UF membranes significantly reduces the water contact angle (WCA) from 77.1° to 24.1°, reflecting increased surface hydrophilicity. This is due to the introduction of oxygen-containing polar groups such as hydroxyl and carboxyl groups, which enhance water affinity and reduce interfacial resistance. As a result, water flux increases from 25.2 to 350.7 $L{\cdot}m^{-2}{\cdot}h^{-1}$. BSA rejection improves from 55 to 99.9 %, and fouling resistance rises from 50 to 82 % [71]. Carboxybetaine-functionalized

Table 1
Comparison table of performance of ppAAc/PSf membrane membranes with literature.

Process	Modification	Property	Plasma modified membrane	Pristine membrane	Ref
UF	Ar/O_2 plasma (PSF membrane)	WCA	24.1°	77.1°	[71]
		Flux	350.7 $L{\cdot}m^{-2}{\cdot}h^{-1}$	25.2 $L{\cdot}m^{-2}{\cdot}h^{-1}$	
		Fouling resistance	82 %	50 %	
		BSA rejection	99.90 %	55 %	
UF	Carboxybetane (PE membrane)	BSA adsorption	0.023 mg/cm^2 (24 h)	0.096 mg/cm^2 (24 h)	[72]
FO	AAc + Ar (cellulose triacetate)	WCA	36.4°	64°	[73]
		Flux	8.12 $L{\cdot}m^{-2}{\cdot}h^{-1}$	6.11 $L{\cdot}m^{-2}{\cdot}h^{-1}$	
		Protein recovery	10.10 %	4 %	
NF	NH_3 plasma (commercial TFC)	WCA	12.1°	78°	[74]
		Salt rejection	95 %	85 %	
		Flux	1.4 $L{\cdot}m^{-2}{\cdot}h^{-1}{\cdot}bar^{-1}$	1 $L{\cdot}m^{-2}{\cdot}h^{-1}{\cdot}bar^{-1}$	
		BSA adsorption	0.22 mg/mg membrane	0.38 mg/mg membrane	
RO	Vinylimidazole (TFC)	Flux	49.2 $L{\cdot}m^{-2}{\cdot}h^{-1}$	44.9 $L{\cdot}m^{-2}{\cdot}h^{-1}$	[43]
		Salt rejection	97 %	98 %	
UF	HMDSO (PET membrane)	WCA	10°	140°	[75]
UF	ppAAc-coated (PSf membrane)	WCA	15.1°	73.3°	This work
		Permeance	25 $L{\cdot}m^{-2}{\cdot}h^{-1}{\cdot}bar^{-1}$	200 $L{\cdot}m^{-2}{\cdot}h^{-1}{\cdot}bar^{-1}$	
		PFAS rejection	80–98 %	60–78 %	

polyethylene membranes also show a reduction in BSA adsorption from 0.096 to 0.023 mg/cm^2, attributed to zwitterionic groups forming a strong hydration layer that resists protein attachment [72].

In FO, membranes modified with acrylic acid (AAc) and argon plasma show increased hydrophilicity, with WCA decreasing from 64° to 36.4°. This modification enhances water transport, raising flux from 6.11 to 8.12 L·m^{-2}·h^{-1} and improving protein recovery from 4 to 10.1 % [73]. In NF, low-pressure ammonia plasma introduces amine groups and raises surface energy, lowering the WCA from 78° to 12.1°. These changes increase salt rejection from 85 to 95 % and reduce BSA adsorption from 0.38 to 0.22 mg/mg membrane, while flux increases from 1.0 to 1.4 L·m^{-2}·h^{-1}·bar^{-1} [74]. Similarly, RO membranes coated with vinylimidazole demonstrate an increase in flux from 44.9 to 49.2 L·m^{-2}·h^{-1} while maintaining high salt rejection between 97 % and 98 %, likely due to enhanced hydrophilicity and preserved membrane integrity [43]. UF membranes modified with hydrophobic HMDSO exhibit a sharp reduction in WCA from 140° to 10°, indicating a significant improvement in surface wettability caused by plasma-induced surface restructuring [75,76].

Meanwhile, ppAAc-coated PSf membranes prepared in the present work achieve higher PFAS rejection, increasing from a range of 60–78 % up to 80–98 %. This improvement is accompanied by a drop in WCA from 73.3° to 15.1°, and a decrease in pure water permeance from 200 to 25 L·m^{-2}·h^{-1}·bar^{-1}, indicating a tighter and more selective membrane surface. These enhancements result from targeted surface functionalization and controlled morphology provided by plasma processes, which together optimize membranes for high-performance separations [77].

4. Conclusions and prospects

Plasma polymerization proved to be a versatile and environmentally friendly approach for fabricating effective filtration barrier layers, particularly by lowering the molecular weight cut-off (MWCO) to enable high rejection of per- and polyfluoroalkyl substances (PFAS) with molecular weights above 500 Da. By tuning plasma energy input, the degree of cross-linking and polymer film density could be controlled, allowing membranes with tailored selectivity, permeability, and fouling resistance optimized for PFAS separation. The optimized ppAAc/PSf membranes achieved PFAS rejection of 86–100 % depending on the compound, with DI water permeance reduced by up to ~87 % for the most cross-linked films, reflecting enhanced barrier performance. Plasma treatment also imparted a strongly hydrophilic and negatively charged surface, minimizing PFAS adsorption despite their hydrophobic nature. Systematic filtration experiments and high-resolution synchrotron-FTIR mapping revealed that PFAS with higher molecular weights and longer fluorocarbon chains exhibited stronger interactions with the membrane, contributing to surface adsorption and internal fouling. These findings emphasize the importance of both membrane surface chemistry and PFAS physicochemical properties for effective removal. Overall, the ppAAc-modified PSf membranes show significant potential for advanced water purification and can be further explored for selective removal of a broader range of contaminants, supporting sustainable water treatment and reuse applications.

CRediT authorship contribution statement

Jingshi Wang: Writing – original draft, Methodology, Formal analysis, Data curation. **Priyanka Kumari:** Writing – review & editing, Formal analysis, Data curation. **Jitraporn Vongsvivut:** Writing – review & editing, Supervision, Methodology, Investigation. **Andrea Merenda:** Writing – review & editing, Methodology, Formal analysis. **Jiangting Wang:** Writing – review & editing, Investigation, Formal analysis. **Zhiqiang Chen:** Writing – review & editing, Supervision, Methodology. **Ilana Timokhina:** Writing – review & editing, Supervision, Formal analysis. **Ludovic F. Dumée:** Writing – review & editing, Writing – original draft, Investigation, Formal analysis. **Lingxue Kong:** Writing – review & editing, Supervision, Data curation.

Declaration of competing interest

Ludovic F. DUMEE has been an editor of the Journal of Water Process Engineering since July 2019. He was not involved with neither the review process nor the handling of paper.

Acknowledgement

Dr. Jingshi Wang thanks the kind provision of her top-up AINSE/ANSTO scholarship and support from the Australian Synchrotron. The authors acknowledge the facilities and the technical assistance of the RMIT University's Microscopy and Microanalysis Facility (RMMF).

Appendix A. Supplementary data

Supplementary data to this article can be found online at https://doi.org/10.1016/j.jwpe.2025.108635.

Data availability

Data will be made available on request.

References

[1] S.P. Lenka, M. Kah, L.P. Padhye, A review of the occurrence, transformation, and removal of poly- and perfluoroalkyl substances (PFAS) in wastewater treatment plants, Water Res. 199 (2021) 117187, https://doi.org/10.1016/j.watres.2021.117187.
[2] W.N. Zhang, P.P. Cheng, J. Cheng, N. Li, Y. Wang, J.Y. Yang, X.Y. Qiu, H. Tan, H. Z. Yu, Ultrathin nanoporous membrane fabrication based on block copolymer micelles, J. Membr. Sci. 570 (2019) 427–435, https://doi.org/10.1016/j.memsci.2018.10.066.
[3] Y. Yin, Y. Zhao, C. Li, R. Wang, Fabrication of polyamide hollow fiber nanofiltration membrane with intensified positive surface charge density via a secondary interfacial polymerization, J. Membr. Sci. 682 (2023) 121778, https://doi.org/10.1016/j.memsci.2023.121778.
[4] D. Li, H. Wang, Recent developments in reverse osmosis desalination membranes, J. Mater. Chem. 20 (22) (2010) 4551–4566.
[5] E. Dražević, K. Košutić, V. Freger, Permeability and selectivity of reverse osmosis membranes: correlation to swelling revisited, Water Res. 49 (2014) 444–452, https://doi.org/10.1016/j.watres.2013.10.029.
[6] H. Chen, W.-S. Hung, C.-H. Lo, S.-H. Huang, M.-L. Cheng, G. Liu, K.-R. Lee, J.-Y. Lai, Y.-M. Sun, C.-C. Hu, R. Suzuki, T. Ohdaira, N. Oshima, Y.C. Jean, Free-volume depth profile of polymeric membranes studied by positron annihilation spectroscopy: layer structure from interfacial polymerization, Macromolecules 40 (21) (2007) 7542–7557, https://doi.org/10.1021/ma071493w.
[7] M. Ulbricht, Advanced functional polymer membranes, Polymer 47 (7) (2006) 2217–2262, https://doi.org/10.1016/j.polymer.2006.01.084.
[8] J.G. Wijmans, R.W. Baker, The solution-diffusion model: a review, J. Membr. Sci. 107 (1) (1995) 1–21, https://doi.org/10.1016/0376-7388(95)00102-I.
[9] F. DOW, Reverse osmosis membranes technical manual. http://msdssearch.dow.com/PublishedLiteratureDOWCOM/dh_095b/0901b8038095b91d.pdf?filepath=/609-00071.pdf&fromPage=GetDoc, 2003. (Accessed July 2017).
[10] S. Karan, S. Samitsu, X. Peng, K. Kurashima, I. Ichinose, Ultrafast viscous permeation of organic solvents through diamond-like carbon nanosheets, Science 335 (6067) (2012) 444–447.
[11] S. Karan, Z. Jiang, A.G. Livingston, Sub–10 nm polyamide nanofilms with ultrafast solvent transport for molecular separation, Science 348 (6241) (2015) 1347–1351.
[12] F.-M. Allioux, C.J. Garvey, C. Rehm, B.L. Tardy, R.R. Dagastine, P.D. Hodgson, L. Kong, L.F. Dumée, Insights into free volume variations across ion-exchange membranes upon mixed solvents uptake by small and ultrasmall angle neutron scattering, ACS Appl. Mater. Interfaces 9 (10) (2017) 8704–8713, https://doi.org/10.1021/acsami.6b15958.
[13] I.R. Marques, M.J.L. Leite, A.M. Piacentini, C. Binder, M.E.R. Dotto, A. Ambrosi, M. Di Luccio, C. da Costa, Improved performance of the ultrafiltration membranes by simple modification with air plasma treatment and polymeric deposition, J. Appl. Polym. Sci. 141 (19) (2024) e55341, https://doi.org/10.1002/app.55341.
[14] A. Yusuf, A. Sodiq, A. Giwa, J. Eke, O. Pikuda, G. De Luca, J.L. Di Salvo, S. Chakraborty, A review of emerging trends in membrane science and technology for sustainable water treatment, J. Clean. Prod. 266 (2020) 121867, https://doi.org/10.1016/j.jclepro.2020.121867.
[15] B.S. Lalia, V. Kochkodan, R. Hashaikeh, N. Hilal, A review on membrane fabrication: structure, properties and performance relationship, Desalination 326 (2013) 77–95, https://doi.org/10.1016/j.desal.2013.06.016.

[16] A.K. Hołda, I.F.J. Vankelecom, Understanding and guiding the phase inversion process for synthesis of solvent resistant nanofiltration membranes, J. Appl. Polym. Sci. 132 (27) (2015), https://doi.org/10.1002/app.42130.
[17] T. Wu, H. Wu, X. Feng, S. Luo, M. Wu, Y. Zhang, High-flux polyamide nanofiltration membranes via phosphate saline-buffered polymerization, J. Membr. Sci. 681 (2023) 121770, https://doi.org/10.1016/j.memsci.2023.121770.
[18] S.T. M, A.B. Arshad, P.T. Lin, J. Widakdo, M.H. K, H.F.M. Austria, C.-C. Hu, J.-Y. Lai, W.-S. Hung, A review of recent progress in polymeric electrospun nanofiber membranes in addressing safe water global issues, RSC Adv. 11 (16) (2021) 9638–9663, https://doi.org/10.1039/D1RA00060H.
[19] L. Guo, Y. Wang, M. Steinhart, Porous block copolymer separation membranes for 21st century sanitation and hygiene, Chem. Soc. Rev. 50 (11) (2021) 6333–6348, https://doi.org/10.1039/D0CS00500B.
[20] D.A. Joshi, N., An overview on common organic solvents and their toxicity, J. Pharm. Res. Int. 28 (2019) 1–18, https://doi.org/10.9734/jpri/2019/v28i330203.
[21] E.S. Liubimova, A.V. Bildyukevich, G.B. Melnikova, V.V. Volkov, Modification of hollow fiber ultrafiltration membranes by interfacial polycondensation: monomer ratio effect, Pet. Chem. 55 (10) (2015) 795–802, https://doi.org/10.1134/S0965544115100138.
[22] S.Z.F. Fadhillah, Application of Multilayer Thin Film Technology in Desalination Membrane, InTech, 2017.
[23] M.S. Kang, B. Chun, S.S. Kim, Surface modification of polypropylene membrane by low-temperature plasma treatment, J. Appl. Polym. Sci. 81 (6) (2001) 1555–1566, https://doi.org/10.1002/app.1585.
[24] H.I. Kim, S.S. Kim, Fabrication of reverse osmosis membrane via low temperature plasma polymerization, J. Membr. Sci. 190 (1) (2001) 21–33, https://doi.org/10.1016/S0376-7388(01)00380-5.
[25] A.K. Wardani, Organic fouling mechanism in ultrafiltration membrane for drinking water, AIP Conf. Proc. 3073 (1) (2024) 070009, https://doi.org/10.1063/5.0193627.
[26] R. Reis, L.F. Dumée, L. He, F. She, J.D. Orbell, B. Winther-Jensen, M.C. Duke, Amine enrichment of thin-film composite membranes via low pressure plasma polymerization for antimicrobial adhesion, ACS Appl. Mater. Interfaces 7 (27) (2015) 14644–14653, https://doi.org/10.1021/acsami.5b01603.
[27] X.J. Dai, J.d. Plessis, I.L. Kyratzis, G. Maurdev, M.G. Huson, C. Coombs, Controlled amine functionalization and hydrophilicity of a poly(lactic acid) fabric, Plasma Process. Polym. 6 (8) (2009) 490–497, https://doi.org/10.1002/ppap.200800216.
[28] F. Turgut, C.Y. Chong, M. Karaman, W.J. Lau, M. Gürsoy, A.F. Ismail, Plasma surface modification of graphene oxide nanosheets for the synthesis of GO/PES nanocomposite ultrafiltration membrane for enhanced oily separation, J. Appl. Polym. Sci. 140 (5) (2023) e53410, https://doi.org/10.1002/app.53410.
[29] A. Ghodsi, H. Fashandi, Contribution of graphene oxide (GO)-containing polydimethylsiloxane (PDMS) binder to the surface modification of electrospun PVDF membrane towards development of photothermal vacuum membrane distillation (PVMD), Sep. Purif. Technol. 348 (2024) 127744, https://doi.org/10.1016/j.seppur.2024.127744.
[30] V. Moghimifar, A. Raisi, A. Aroujalian, Surface modification of polyethersulfone ultrafiltration membranes by corona plasma-assisted coating TiO2 nanoparticles, J. Membr. Sci. 461 (2014) 69–80, https://doi.org/10.1016/j.memsci.2014.02.012.
[31] X. Chen, G. Huang, C. An, R. Feng, Y. Yao, S. Zhao, C. Huang, Y. Wu, Plasma-induced poly(acrylic acid)-TiO2 coated polyvinylidene fluoride membrane for produced water treatment: synchrotron X-ray, optimization, and insight studies, J. Clean. Prod. 227 (2019) 772–783, https://doi.org/10.1016/j.jclepro.2019.04.226.
[32] Y. Yi, H. Tu, X. Zhou, R. Liu, Y. Wu, D. Li, Q. Wang, X. Shi, H. Deng, Acrylic acid-grafted pre-plasma nanofibers for efficient removal of oil pollution from aquatic environment, J. Hazard. Mater. 371 (2019) 165–174, https://doi.org/10.1016/j.jhazmat.2019.02.085.
[33] V.A. Maske, A.M. Kokate, P.A. More, R.S. Salunkhe, A.P. More, A comprehensive review of polyacrylonitrile membranes: modifications and applications, Polym. Bull. 81 (18) (2024) 16415–16455, https://doi.org/10.1007/s00289-024-05508-2.
[34] J. Wang, L. Nie, C. Zhang, B. Wang, Low-pressure air plasma-assisted acrylic grafted polyetherimide ultrafiltration membranes with excellent oil-water separation and high anti-fouling performances, Mater Today Commun 35 (2023) 106325, https://doi.org/10.1016/j.mtcomm.2023.106325.
[35] Y. Chen, J. Zhang, Y. Cohen, Fouling resistant and performance tunable ultrafiltration membranes via surface graft polymerization induced by atmospheric pressure air plasma, Sep. Purif. Technol. 286 (2022) 120490, https://doi.org/10.1016/j.seppur.2022.120490.
[36] Z.F. Gao, G.M. Shi, Y. Cui, T.-S. Chung, Organic solvent nanofiltration (OSN) membranes made from plasma grafting of polyethylene glycol on cross-linked polyimide ultrafiltration substrates, J. Membr. Sci. 565 (2018) 169–178, https://doi.org/10.1016/j.memsci.2018.08.019.
[37] J. Wang, X. Chen, R. Reis, Z. Chen, N. Milne, B. Winther-Jensen, L. Kong, L. F. Dumée, Plasma modification and synthesis of membrane materials—a mechanistic review, Membranes 8 (3) (2018), https://doi.org/10.3390/membranes8030056.
[38] E. Zolghadr, M.D. Firouzjaei, G. Amouzandeh, P. LeClair, M. Elliott, The role of membrane-based technologies in environmental treatment and reuse of produced water, Front. Environ. Sci. 9 (2021) (2021), https://doi.org/10.3389/fenvs.2021.629767.
[39] L. Li, X.J. Dai, H.S. Xu, J.H. Zhao, P. Yang, G. Maurdev, J. du Plessis, P.R. Lamb, B. L. Fox, W.P. Michalski, Combined continuous wave and pulsed plasma modes: for more stable interfaces with higher functionality on metal and semiconductor surfaces, Plasma Process. Polym. 6 (10) (2009) 615–619, https://doi.org/10.1002/ppap.200900042.
[40] L. Dumée, V. Germain, K. Sears, J. Schütz, N. Finn, M. Duke, S. Cerneaux, D. Cornu, S. Gray, Enhanced durability and hydrophobicity of carbon nanotube bucky paper membranes in membrane distillation, J. Membr. Sci. 376 (1) (2011) 241–246, https://doi.org/10.1016/j.memsci.2011.04.024.
[41] F.J. Giessibl, Y. Sugawara, S. Morita, H. Hosoi, K. Sueoka, K. Mukasa, A. Sasahara, H. Onishi, Noncontact atomic force microscopy and related topics, in: B. Bhushan (Ed.), Nanotribology and Nanomechanics I: Measurement Techniques and Nanomechanics, Springer Berlin Heidelberg, Berlin, Heidelberg, 2011, pp. 195–237, https://doi.org/10.1007/978-3-642-15283-2_5.
[42] J. Vongsvivut, D. Perez-Guaita, B.R. Wood, P. Heraud, K. Khambatta, D. Hartnell, M.J. Hackett, M.J. Tobin, Synchrotron macro ATR-FTIR microspectroscopy for high-resolution chemical mapping of single cells, Analyst 144 (10) (2019) 3226–3238, https://doi.org/10.1039/c8an01543k.
[43] R. Reis, M. Duke, A. Merenda, B. Winther-Jensen, L. Puskar, M.J. Tobin, J. D. Orbell, L.F. Dumée, Customizing the surface charge of thin-film composite membranes by surface plasma thin film polymerization, J. Membr. Sci. 537 (2017) 1–10, https://doi.org/10.1016/j.memsci.2017.05.013.
[44] W. Chen, Y. Su, J. Peng, Y. Dong, X. Zhao, Z. Jiang, Engineering a robust, versatile amphiphilic membrane surface through forced surface segregation for ultralow flux-decline, Adv. Funct. Mater. 21 (1) (2011) 191–198, https://doi.org/10.1002/adfm.201001384.
[45] E.F. Castro Vidaurre, C.A. Achete, F. Gallo, D. Garcia, R. Simão, A.C. Habert, Surface modification of polymeric materials by plasma treatment, Mater. Res. 5 (2002) 37–41.
[46] S. Hwang, H. Seo, D.C. Jeong, L. Wen, J.G. Han, C. Song, Y. Kim, Growth kinetics of plasma-polymerized films, Sci. Rep. 5 (2015) 11201, https://doi.org/10.1038/srep11201.
[47] D.S. Wavhal, E.R. Fisher, Modification of polysulfone ultrafiltration membranes by CO2 plasma treatment, Desalination 172 (2) (2005) 189–205, https://doi.org/10.1016/j.desal.2004.06.201.
[48] Z. Zheng, W. Wang, X. Huang, W. Fan, L. Li, Surface modification of polysulfone hollow fiber membrane for extracorporeal membrane oxygenator using low-temperature plasma treatment, Plasma Process. Polym. 15 (1) (2018) 1700122, https://doi.org/10.1002/ppap.201700122.
[49] H. Yasuda, T. Yasuda, The competitive ablation and polymerization (CAP) principle and the plasma sensitivity of elements in plasma polymerization and treatment, J. Polym. Sci. A Polym. Chem. 38 (6) (2000) 943–953, https://doi.org/10.1002/(SICI)1099-0518(20000315)38:6<943::AID-POLA3>3.0.CO;2-3.
[50] J. Friedrich, Mechanisms of plasma polymerization - reviewed from a chemical point of view, Plasma Process. Polym. 8 (9) (2011) 783–802, https://doi.org/10.1002/ppap.201100038.
[51] T. Dufour, From basics to frontiers: a comprehensive review of plasma-modified and plasma-synthesized polymer films, Polymers 15 (17) (2023) 3607.
[52] M.R. Chashmejahanbin, A. Salimi, A. Ershad Langroudi, The study of the coating adhesion on PP surface modified in different plasma/acrylic acid solution, Int. J. Adhes. Adhes. 49 (2014) 44–50, https://doi.org/10.1016/j.ijadhadh.2012.09.008.
[53] H. Dvořáková, J. Čech, M. Stupavská, L. Prokeš, J. Jurmanová, V. Buršíková, J. Ráheľ, P. Sťahel, Fast surface hydrophilization via atmospheric pressure plasma polymerization for biological and technical applications, Polymers 11 (10) (2019) 1613.
[54] J. Garcia-Torres, D. Sylla, L. Molina, E. Crespo, J. Mota, L. Bautista, Surface modification of cellulosic substrates via atmospheric pressure plasma polymerization of acrylic acid: structure and properties, Appl. Surf. Sci. 305 (2014) 292–300, https://doi.org/10.1016/j.apsusc.2014.03.065.
[55] D. Gerchman, B. Bones, M.B. Pereira, A.S. Takimi, Thin film deposition by plasma polymerization using d-limonene as a renewable precursor, Prog. Org. Coat. 129 (2019) 133–139, https://doi.org/10.1016/j.porgcoat.2019.01.018.
[56] J. Wang, X. Chen, R. Reis, Z. Chen, N. Milne, B. Winther-Jensen, L. Kong, L. Dumée, Plasma modification and synthesis of membrane materials—a mechanistic review, Membranes 8 (3) (2018) 56.
[57] I.S. Bae, S.H. Cho, S.B. Lee, Y. Kim, J.H. Boo, Growth of plasma-polymerized thin films by PECVD method and study on their surface and optical characteristics, Surf. Coat. Technol. 193 (1) (2005) 142–146, https://doi.org/10.1016/j.surfcoat.2004.07.022.
[58] R. Jafari, M. Tatoulian, F. Arefi-Khonsari, Improvement of the stability of plasma polymerized acrylic acid coating deposited on PS beads in a fluidized bed reactor, React. Funct. Polym. 71 (4) (2011) 520–524, https://doi.org/10.1016/j.reactfunctpolym.2011.01.012.
[59] M. Shen, S. Keten, R.M. Lueptow, Dynamics of water and solute transport in polymeric reverse osmosis membranes via molecular dynamics simulations, J. Membr. Sci. 506 (2016) 95–108, https://doi.org/10.1016/j.memsci.2016.01.051.
[60] X. Shen, Y. Gao, Y. He, Y. Zhao, L. Chen, Preparation and anti-fouling property of carboxybetaine-based zwitterionic PVDF membrane, Sep. Sci. Technol. 51 (7) (2016) 1189–1198, https://doi.org/10.1080/01496395.2016.1146299.
[61] K. Li, L. Liu, H. Wu, S. Li, C. Yu, Y. Zhou, W. Huang, D. Yan, Understanding the temperature effect on transport dynamics and structures in polyamide reverse osmosis system via molecular dynamics simulations, Phys. Chem. Chem. Phys. 20 (47) (2018) 29996–30005, https://doi.org/10.1039/C8CP05825C.
[62] DuPont, FILMTEC™ BW30-400 High Rejection, High Surface Area Brackish Water RO Element, 2019.
[63] C. Boo, Y. Wang, I. Zucker, Y. Choo, C.O. Osuji, M. Elimelech, High performance nanofiltration membrane for effective removal of perfluoroalkyl substances at high

water recovery, Environ. Sci. Technol. 52 (13) (2018) 7279–7288, https://doi.org/10.1021/acs.est.8b01040.
[64] W. Chen, X. Zhang, M. Mamadiev, Z. Wang, Sorption of perfluorooctane sulfonate and perfluorooctanoate on polyacrylonitrile fiber-derived activated carbon fibers: in comparison with activated carbon, RSC Adv. 7 (2) (2017) 927–938, https://doi.org/10.1039/C6RA25230C.
[65] K. Sookhak Lari, G.B. Davis, A. Kumar, J.L. Rayner, X.-Z. Kong, M.O. Saar, The dynamics of per- and polyfluoroalkyl substances (PFAS) at interfaces in porous media: a computational roadmap from nanoscale molecular dynamics simulation to macroscale modeling, ACS Omega 9 (5) (2024) 5193–5202, https://doi.org/10.1021/acsomega.3c09201.
[66] X. Chen, A. Vanangamudi, J. Wang, J. Jegatheesan, V. Mishra, R. Sharma, S. R. Gray, J. Kujawa, W. Kujawski, F. Wicaksana, L.F. Dumée, Direct contact membrane distillation for effective concentration of perfluoroalkyl substances – impact of surface fouling and material stability, Water Res. 182 (2020) 116010, https://doi.org/10.1016/j.watres.2020.116010.
[67] S. Abdikheibari, L.F. Dumée, V. Jegatheesan, Z. Mustafa, P. Le-Clech, W. Lei, K. Baskaran, Natural organic matter removal and fouling resistance properties of a boron nitride nanosheet-functionalized thin film nanocomposite membrane and its impact on permeate chlorine demand, J Water Process Eng 34 (2020) 101160, https://doi.org/10.1016/j.jwpe.2020.101160.
[68] P. Sen, T. Das, S. Ghosh, A. Sanyal, U. Ghorai, R. Dutta, D. Thapliyal, R.K. Arya, Enhancing the Performance of Ultrafiltration (UF) Membranes with the Aid of Functional Coatings, Functional Coatings for Biomedical, Energy, and Environmental Applications, 2024, pp. 429–466, https://doi.org/10.1002/9781394263172.ch18.
[69] C.Y. Tang, Q.S. Fu, C.S. Criddle, J.O. Leckie, Effect of flux (transmembrane pressure) and membrane properties on fouling and rejection of reverse osmosis and nanofiltration membranes treating Perfluorooctane sulfonate containing wastewater, Environ. Sci. Technol. 41 (6) (2007) 2008–2014, https://doi.org/10.1021/es062052f.
[70] C.Y. Tang, Q. Shiang Fu, D. Gao, C.S. Criddle, J.O. Leckie, Effect of solution chemistry on the adsorption of perfluorooctane sulfonate onto mineral surfaces, Water Res. 44 (8) (2010) 2654–2662, https://doi.org/10.1016/j.watres.2010.01.038.
[71] S.T. Kassa, C.C. Hu, D.L. Keshebo, M. Belle Marie Ang, J.Y. Lai, J.P. Chu, Surface modification of high-rejection ultrafiltration membrane with antifouling capability using activated oxygen treatment and metallic glass deposition, Appl. Surf. Sci. 529 (2020) 147131, https://doi.org/10.1016/j.apsusc.2020.147131.
[72] K. Akamatsu, W. Noto, H. Fukuzawa, A. Hara, S.-i. Nakao, Grafting of carboxybetaine polymers to polyethylene membranes via plasma graft polymerization to improve low-fouling properties and to tune the molecular weight cut-off, Sep. Purif. Technol. 204 (2018) 298–303, https://doi.org/10.1016/j.seppur.2018.05.004.
[73] W. Khongnakorn, W. Bootluck, P. Jutaporn, Surface modification of FO membrane by plasma-grafting polymerization to minimize protein fouling, J Water Process Eng 38 (2020) 101633, https://doi.org/10.1016/j.jwpe.2020.101633.
[74] E.-S. Kim, Q. Yu, B. Deng, Plasma surface modification of nanofiltration (NF) thin-film composite (TFC) membranes to improve anti organic fouling, Appl. Surf. Sci. 257 (23) (2011) 9863–9871, https://doi.org/10.1016/j.apsusc.2011.06.059.
[75] C. Ma, L. Wang, A. Nikiforov, Y. Onyshchenko, P. Cools, K. Ostrikov, N. De Geyter, R. Morent, Atmospheric-pressure plasma assisted engineering of polymer surfaces: from high hydrophobicity to superhydrophilicity, Appl. Surf. Sci. 535 (2021) 147032, https://doi.org/10.1016/j.apsusc.2020.147032.
[76] S. Liang, Z. Ma, Z. Fan, M. Gu, H. Ding, D. Wu, Y. Gao, X. Huang, Tuning membrane surface wetting behavior via dual-nanomaterial functionalization for efficient water purification, J. Membr. Sci. 724 (2025) 123970, https://doi.org/10.1016/j.memsci.2025.123970.
[77] A.O. Rashed, C. Huynh, A. Merenda, S. Qin, M. Maghe, L. Kong, T. Kondo, L. F. Dumée, J.M. Razal, Carbon nanofibre microfiltration membranes tailored by oxygen plasma for electrocatalytic wastewater treatment in cross-flow reactors, J. Membr. Sci. 673 (2023) 121475, https://doi.org/10.1016/j.memsci.2023.121475.